Diagnosing Flavors of Tropospheric Rossby Wave Breaking and Their Associated Dynamical and Sensible Weather Features

GRANT LACHAT,[a] KEVIN A. BOWLEY,[a] AND MELISSA GERVAIS[a,b]

[a] *Department of Meteorology and Atmospheric Science, The Pennsylvania State University, University Park, Pennsylvania*
[b] *Institute for Computational and Data Sciences, The Pennsylvania State University, University Park, Pennsylvania*

(Manuscript received 22 July 2023, in final form 15 November 2023, accepted 8 December 2023)

ABSTRACT: Rossby wave breaking (RWB) can be manifested by the irreversible overturning of isentropes on constant potential vorticity (PV) surfaces. Traditionally, the type of breaking is categorized as anticyclonic (AWB) or cyclonic (CWB) and can be identified using the orientation of streamers of high potential temperature (θ) and low θ air on a PV surface. However, an examination of the differences in RWB structure and their associated tropospheric impacts within these types remains unexplored. In this study, AWB and CWB are identified from overturning isentropes on the dynamic tropopause (DT), defined as the 2 potential vorticity unit (PVU; 1 PVU = 10^{-6} K kg^{-1} m^2 s^{-1}) surface, in the ERA5 dataset during December, January, and February 1979–2019. Self-organizing maps (SOM), a machine learning method, is used to cluster the identified RWB events into archetypal patterns, or "flavors," for each type. AWB and CWB flavors capture variations in the θ minima/maxima of each streamer and the localized meridional θ gradient ($\nabla\theta$) flanking the streamers. Variations in the magnitude and position of $\nabla\theta$ between flavors correspond to a diversity of jet structures leading to differences in vertical motion patterns and troposphere-deep circulations. A subset of flavors of AWB (CWB) events are associated with the development of strong surface high (low) pressure systems and the generation of extreme poleward moisture transport. For CWB, many events occurred in similar geographical regions, but the precipitation and moisture patterns were vastly different between flavors. Our findings suggest that the location, type, and severity of the tropospheric impacts from RWB are strongly dictated by RWB flavor.

SIGNIFICANCE STATEMENT: Large-scale atmospheric waves ~15 km above Earth's surface are responsible for the daily weather patterns that we experience. These waves can undergo wave breaking, a process that is analogous to ocean waves breaking along the seashore. Wave breaking events have been linked to extreme weather impacts at the surface including cold and heat waves, strong low pressure systems, and extreme precipitation events. Machine learning is used to identify and analyze different flavors, or patterns, of wave breaking events that result in differing surface weather impacts. Some flavors are able to generate notable channels of moisture that result in extreme high precipitation events. This is a crucial insight as forecasting of extreme weather events could be improved from this work.

KEYWORDS: Dynamics; Potential vorticity; Rossby waves; Wave breaking; Machine learning

1. Introduction

Rossby wave breaking (RWB) has been a phenomenon of considerable interest due to its connection to extreme weather events (e.g., Liu and Barnes 2015; Hu et al. 2017; Röthlisberger et al. 2019) and mid- and high-latitude blocking (e.g., Tyrlis and Hoskins 2008; Woods et al. 2013; Liu and Barnes 2015; Röthlisberger et al. 2019) among other phenomena. RWB is manifested by the overturning and irreversible deformation of isentropes on constant potential vorticity (PV) surfaces (McIntyre and Palmer 1983) that occur when the phase speed of a Rossby wave matches the speed of the background flow (Polvani and Plumb 1992). These overturning isentropes generally present as poleward and equatorward displacements, or streamers (e.g., Appenzeller et al. 1996; Wernli and Sprenger 2007), of high and low potential temperature (θ) air, respectively. The alignment of these high θ and low θ streamers is dictated by the horizontal wind shear generated by the jet stream and has been used to broadly classify RWB as anticyclonic (LC1, P2, AWB) or cyclonic (LC2, P1, CWB) (e.g., Thorncroft et al. 1993; Peters and Waugh 1996; Bowley et al. 2019a). The difference between the P-type and LC-naming conventions are based on the RWB event initiation, where LC events initiate from the equatorward trough of the +PV streamer and the P-type events initiate from the poleward intruding streamer of −PV air (Thorncroft et al. 1993; Peters and Waugh 1996). The AWB and CWB designation is not dependent on the component of the precursor wave that undergoes breaking (e.g., Bowley et al. 2019a). Though the broader event categories have been well explored, differences in the patterns and shapes of these streamers within each RWB category (i.e., AWB or CWB) and their importance for associated sensible weather impacts remain largely uninvestigated.

The climatology of Northern Hemisphere RWB frequencies has been well studied and there is general agreement on regions of more frequent tropospheric RWB activity, or "surf zones" (e.g., Postel and Hitchman 1999; Waugh and Polvani 2000;

Denotes content that is immediately available upon publication as open access.

Supplemental information related to this paper is available at the Journals Online website: https://doi.org/10.1175/MWR-D-23-0153.s1.

Corresponding author: Grant LaChat, glachat@psu.edu

DOI: 10.1175/MWR-D-23-0153.1

Hitchman and Huesmann 2007; Martius et al. 2007; Bowley et al. 2019a). AWB surf zones during December–February (DJF) are located over the North Pacific (~25°–45°N, 180°–110°W) and eastern North Atlantic (~35°–55°N, 60°W–10°E) Ocean basins (e.g., Martius et al. 2007; Strong and Magnusdottir 2008; Bowley et al. 2019a). The surf zones for CWB during DJF are shifted farther west and north across the central Pacific (~50°–65°N, 160°E–140°W) and central North Atlantic (~55°–70°N, 65°–25°W) basins (Waugh and Polvani 2000; Strong and Magnusdottir 2008; Bowley et al. 2019a). During DJF, AWB is more frequent than CWB and there are more RWB (i.e., AWB and CWB) events in the Atlantic than the Pacific basin (Abatzoglou and Magnusdottir 2006; Strong and Magnusdottir 2008; Bowley et al. 2019a).

Fewer studies have analyzed individual RWB events (e.g., Thorncroft et al. 1993; Masato et al. 2012; Bowley et al. 2019a), RWB-centered composites (Strong and Magnusdottir 2008; Bowley et al. 2019b), or anticyclone-/cyclone-centered composites from RWB events (e.g., Tamarin-Brodsky and Harnik 2023). Generally, these studies have shown that a zonally elongated surface high develops during AWB events and a deep surface cyclone develops during CWB events. These surface features can, through PV arguments, also impact advection of PV on the dynamic tropopause (DT), often defined as the 2.0 potential vorticity unit (PVU) surface where 1 PVU $= 10^{-6}$ K kg^{-1} m^{2} s^{-1} (Hoskins et al. 1985). Given the impacts of RWB on tropospheric circulations, RWB has been connected to episodes of extremely high moisture transport (e.g., Woods et al. 2013; Liu and Barnes 2015; Hu et al. 2017), large precipitation events (e.g., Röthlisberger et al. 2016; de Vries 2021; Michel et al. 2021), extremes in surface temperature (e.g., Masato et al. 2012; Röthlisberger et al. 2019), and outbreaks of Saharan dust (e.g., Dhital et al. 2020), among other phenomena.

The sensible weather extremes associated with RWB are generated, in part, by episodes of atmospheric blocking (e.g., Masato et al. 2012). Therefore, it is crucial to consider how RWB leads to atmospheric blocking episodes. Tyrlis and Hoskins (2008) found that AWB can initiate a blocking pattern by increasing the strength of the planetary ridge across the eastern North Atlantic basin. These events can often result in patterns similar to Rex blocks (Masato et al. 2012). CWB has also been observed as a precursor to blocking over the eastern North Atlantic basin (Tyrlis and Hoskins 2008). Masato et al. (2012) found in composites of DJF AWB (CWB) events that negative (positive) precipitation anomalies were upstream (downstream) of the low θ streamer. Furthermore, negative (positive) 2-m temperature anomalies were collocated with low θ (high θ) streamer for both wave break types. These temperature extremes appear to be driven by persistent surface circulations generated by RWB for many of the blocking events in Masato et al. (2012). Similar RWB-blocking impacts were seen on regional cyclone activity, with North Atlantic basin AWB resulting in decreased cyclone activity and the opposite being true for CWB (Röthlisberger et al. 2016). Although prior work has focused on the sensible weather impacts from blocking initiated by RWB, there has been limited insight on how wave break structure within each RWB event type may influence the development, or maintenance, of the structure of blocking patterns.

Extreme high moisture transport has also been linked to RWB and can have significant regional impacts (e.g., Woods et al. 2013; Liu and Barnes 2015; Hu et al. 2017; de Vries 2021; Michel et al. 2021). RWB events account for a large fraction of high-latitude extreme moisture transport episodes. It has been found that 68% of anonymously large moisture transport episodes poleward of 60°N (Liu and Barnes 2015) and nearly 30% of total moisture transport across 70°N (Woods et al. 2013) are associated with these events. Woods et al. (2013) also found that RWB-influenced moisture transport can explain approximately 40% of the interannual variance of Arctic mean downward longwave radiation. de Vries (2021) observed that RWB events are linked to as many as 70% of extreme precipitation events (EPEs) in the subtropics and midlatitudes, including semiarid regions like the southwest United States and the Middle East. Their study analyzed the concurrence of RWB and spatially large structures of integrated water vapor transport (IWVT), or IWVT structures that resemble atmospheric rivers (ARs). These findings are consistent with Hu et al. (2017), who found that nearly 70% of ARs on the U.S. West Coast are associated with RWB. Understanding the characteristics of RWB structure that lead to the channeling of high IWVT is crucial for determining whether a given RWB event will be associated with an EPE.

It is expected that variations in the shape and intensity of overturning isentropes on the DT (e.g., Papin et al. 2020) will result in changes to the tropospheric-deep circulations initiated by RWB. This can be understood through the context of PV conservation. For AWB (CWB), thermal wind adjustment occurs to restore geostrophic balance which is upset by the advection of $-$PV ($+$PV) air poleward (equatorward). This adjustment by the thermal wind generates an anticyclonic (cyclonic) circulation that extends throughout the depth of the troposphere. Given that the climatological background PV gradient is strongly northward in the upper troposphere, the advection of $-$PV ($+$PV) air from the anticyclonic (cyclonic) circulation reinforces the $-$PV ($+$PV) anomaly at the tropopause through negative (positive) PV advection. This further strengthens the troposphere deep anticyclonic (cyclonic) circulation. These processes leading to advection of PV on the DT are complex and highly interactive. Ultimately, these processes impact the orientation of overturning isentropes on the DT. Therefore, we seek to further understand how differences in the intensity and shape of overturning isentropes on the DT will result in differences in the intensity and position of tropospheric-deep circulations initiated by wave breaking events.

The goal of this study is to identify differences in RWB structure within each RWB type and their associated tropospheric impacts. Following Bowley et al. (2019a), identification of RWB events is completed by searching for instances of overturning isentropes on the DT for the Northern Hemisphere. Event-centered snapshots for each identified RWB event are input into a self-organizing map (SOM), a machine learning method that clusters data into representative patterns. Here, SOM is used to identify a set of patterns, or “flavors” (e.g., Johnson 2013), of AWB and CWB events based on the orientation of overturning isentropes. The mechanisms through which RWB flavors result in different tropospheric deep circulations are identified and we address how RWB flavors can result in different weather impacts.

2. Data and methods

a. Data

The European Centre for Medium-Range Weather Forecasts (ECMWF) Reanalysis version 5 (ERA5) dataset was used in this study (Hersbach et al. 2018). This state-of-the-art dataset is produced within the ECMWF Integrated Forecast System (IFS) from 1940 to the present. Atmospheric variables are available at 137 model levels, a grid spacing of 0.25° × 0.25°, and an hourly temporal resolution. The focus of this work is on Northern Hemisphere RWB events during winter from 1979 to 2019 and analysis was performed on 6-hourly time steps representing instantaneous values at 0000, 0600, 1200, and 1800 UTC of each day. Additionally, the ERA5 data were regridded using a first-order conservative remapping to a lower spatial resolution of 0.90° latitude × 1.25° longitude grid spacing, which acts to smooth the data. This has an additional advantage of enabling a direct comparison of RWB events in the ERA5 to those produced using global climate model simulations such as the Community Earth System Model 2 Large Ensemble (LENS2; Rodgers et al. 2021) that utilizes the same grid spacing.

Potential vorticity (PV) was calculated following McIntyre and Palmer (1983) and Hoskins et al. (1985) as

$$\mathrm{PV} = -g\left[\frac{\partial u}{\partial p}\frac{\partial \theta}{\partial y} - \frac{\partial v}{\partial p}\frac{\partial \theta}{\partial x} + \frac{\partial \theta}{\partial p}(\zeta + f)\right], \qquad (1)$$

where g is the gravitational acceleration (9.81 m s^{-2}), u is the zonal wind (m s^{-1}), v is the meridional wind (m s^{-1}), θ is the potential temperature (K), p is the pressure (Pa), ζ is the relative vorticity (s^{-1}), and f is the Coriolis parameter (s^{-1}). A "top-down" approach was used to search for and linearly interpolate to the highest-altitude 2-PVU surface, or DT, for each time step, as in Bowley et al. (2019a). This method is completed by starting the linear interpolation at the highest altitude (lowest pressure level) and ending at the lowest altitude (highest pressure level). The u, v, T, and p fields were then calculated on the DT, and θ was calculated from these fields. An additional thermodynamic threshold for θ on the DT was utilized to ensure proper representation of the tropopause near the equator. Potential temperature values exceeding 460 K were assigned as missing data since values these large would represent either the stratosphere or tropical tropopause during DJF (Hitchman and Huesmann 2007) which was not of interest in this study.

b. Wave break identification algorithm

A variety of methods have been employed in prior work to identify RWB events. Different coordinate systems have been utilized to identify wave breaking including PV contours on isentropic surfaces (e.g., Postel and Hitchman 1999; Waugh and Polvani 2000; Abatzoglou and Magnusdottir 2006; Wernli and Sprenger 2007), contours of absolute vorticity on isobaric surfaces (e.g., Rivière 2009; Barnes and Hartmann 2012), and isentropes on constant PV surfaces (Benedict et al. 2004; Liu et al. 2014; Bowley et al. 2019a,b). We have chosen the method of Bowley et al. (2019a) that identifies overturning isentropes on the DT. The DT has been demonstrated to be a surface that represents the overturning of material contours associated with RWB events well (Hoskins et al. 1985; Hitchman and Huesmann 2007). Further, the DT responds to changes in the thermodynamic and dynamical features of the environment (Hoskins et al. 1985), making it an ideal surface for comparing RWB on the DT across different time periods (e.g., seasons and years) and latitudes.

Following Bowley et al. (2019a), isentropic contours were identified as overturning if the following criteria were met: (i) The contour continuously encircled the entire hemisphere (to remove PV cutoffs); (ii) The contour crossed the same meridian at least three times (to represent overturning), (iii) the total length of the overturning component of the contour exceeded 1500 km, and (iv) The overturning contour extended across at least 5° but no more than 40° of longitude (to capture synoptic-scale events). A wave break event was identified if three or more overturning contours occurred within 15° great circle distance of each other (Bowley et al. 2019a). The RWB region is identified as the northern-, eastern-, southern-, and western-most points of overturning for the identified contours. Finding RWB events using this method ensures that both the poleward and equatorward components of the RWB are captured as it is not limited to only identifying a region of PV gradient reversal (e.g., Postel and Hitchman 1999; Hitchman and Huesmann 2007) or one of the two PV streamers (e.g., Wernli and Sprenger 2007; Martius et al. 2007), which may be more appropriate for studying specific phenomena. This is a useful quality as we are interested in assessing how differences in RWB structure leads to different tropospheric impacts in this study. Events are typed as AWB if the western (starting) point of an overturning contour is poleward of the eastern (ending) point, and vice versa for CWB. For each event, the RWB algorithm outputs the RWB event type, the bounding region, the geographic center (centroid), and the overturning isentropes. Further discussion of this algorithm can be found in Bowley et al. (2019a).

The RWB event identification algorithm was applied to the Northern Hemisphere DT θ field for each 6-h time step in DJF for the 1979–2019 period to identify instantaneous periods of AWB and CWB (which we hereafter will refer to as a *AWB or CWB event*). Following initial testing with SOM, we identified a subset of RWB events that were occurring at low latitudes on high potential temperature surfaces frequently exceeding 360 K. During DJF, these values are generally representative of the tropical tropopause (Postel and Hitchman 1999; Hitchman and Huesmann 2007) and we are interested in RWB on the extratropical tropopause. Thus, an additional criteria beyond Bowley et al. (2019a) was employed, wherein all RWB events with a mean θ (for all identified overturning isentropes) exceeding 360 K were discarded. This capturing of tropical tropopause cases in the wave break identification algorithm was only discovered after using SOM to identify RWB flavors, indicating that SOM can also be used as a tool for quality control of automated event identification schemes. In total, 21 726 AWB events and 12 567 CWB events were identified throughout the 41-yr period of our study.

c. Self-organizing maps

SOM is an unsupervised, machine learning method that can cluster large datasets into representative spatial patterns

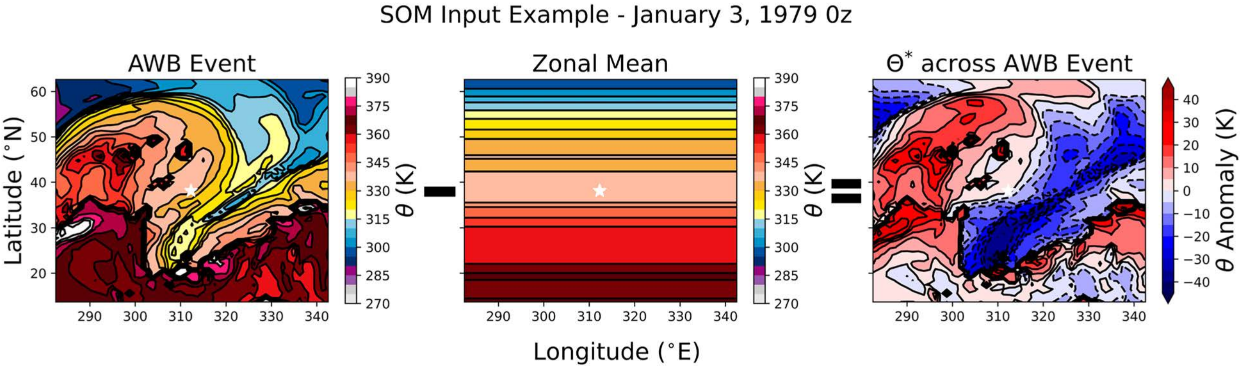

FIG. 1. An example of the preprocessing used to create the input data for the self-organizing maps algorithm. (a) The dynamic tropopause θ field (5-K contour interval; colored and solid black contour) for an identified AWB event across the Atlantic Ocean basin at 0000 UTC 3 Jan 1979. The white star marks the identified centroid of the event. (b) The zonal mean of the AWB event (5-K contour interval; colored and solid black contour). (c) The θ^* (5-K contour interval; colored and dashed and solid contours) calculated by subtracting the event zonal mean from the AWB event. Fields of θ^* were the input data used by the SOM.

(Kohonen 1982). SOM has become increasingly popular within the atmospheric sciences, being used to develop synoptic climatologies (Hewitson and Crane 2002), identify synoptic-scale circulation patterns (Cavazos 2000; Cassano et al. 2006; Schuenemann and Cassano 2010), characterize Northern Hemisphere jet regimes (Gervais et al. 2019; Madsen and Martin 2023), study teleconnection patterns (Johnson et al. 2008), and understand past and future climate variability (Gervais et al. 2016; Gu and Gervais 2021, 2022). SOM analysis was implemented in this study because of the multiple advantages it has over other dimension reduction methods. There is no requirement for orthogonality or linearity in SOM, unlike Empirical Orthogonal Functions (EOFs), which results in patterns that are more physical (Liu et al. 2006; Johnson et al. 2008). Furthermore, mechanisms associated with each SOM node can be diagnosed through composite analysis of additional variables (e.g., Gu and Gervais 2022).

For this study, we used SOM to cluster AWB and CWB events based on the orientation of overturning isentropes. Identified RWB centroids were used to produce 50° latitude × 60° longitude DT θ fields centered on each wave break event. The DT θ fields were preprocessed by removing the individual event field zonal mean (i.e., $\theta^* = \theta - [\theta]$) from each identified AWB or CWB, as illustrated in Fig. 1. The input data used in the SOM were the preprocessed fields of θ^*. Removal of the zonal mean was completed as prior testing of SOM without any preprocessing of the RWB event centered fields revealed that events were being clustered based on the mean background θ state (i.e., latitude). This also aids in removing the impact of seasonality. Additional testing found that using RWB event centered fields with the spatial mean removed resulted in the SOM primarily clustering events on the magnitude of the isentropic gradient, rather than by a combination of the magnitude of gradient and shape of streamer. No criteria for synoptic independence was applied to the input data. This allowed us to capture the full spectrum of instantaneous RWB features that comprise each RWB event type.

SOM nodes, or RWB "flavors," are produced through an iterative process with repeated exposure to the input data of wave break centered DT θ^* fields. First, SOM nodes are initialized with random values that take the shape of the input data. Next, the SOM undergoes two training periods, where the map nodes are adjusted toward the input data according to the following equation:

$$m_i(t + 1) = m_i(t) + \alpha(t)h_{\mathrm{ci}}(t)[x(t) - m_i(t)], \qquad (2)$$

where m_i is the ith map node, $x(t)$ is the input data, and t is the training time step. Here, each input data vector is provided 25 times per training. This results in a total number of 543 150 training steps for the AWB SOM and 314 175 for the CWB SOM. We implement the Epanechikov neighborhood function [$h_{\mathrm{ci}}(t)$], which has been shown to outperform other neighborhood functions (Liu et al. 2006). At each training step the closest SOM node is identified as that with the smallest Euclidean distance to the current input data vector. The neighborhood function acts to produce the greatest modification to the closest SOM node and leaves those outside a defined radius of influence unmodified. As such, it acts to organize the SOM by clustering similar (dissimilar) patterns into neighboring (nonadjacent) SOM nodes. Here, the radius of influence is initially 5 (2) during the first (second) training and linearly decreases to 1 over the training time. The learning rate parameter $\alpha(t)$ determines the extent of the modification of the map nodes and decreases as an inverse function of the training time from initial values of 0.1 and 0.01 for the first and second trainings, respectively. Once the SOM training is complete, the nodes are fixed in place and will be referred to as the RWB flavors. Each input data are assigned to the node with the smallest Euclidean distance, defined as the best matching unit (BMU). The BMUs are then used to compute RWB flavor composites of additional variables.

Of the many user-controllable inputs to the SOM algorithm, the SOM size is one of the most important and subjective. A 3 × 4 SOM was chosen in this study after testing other SOM sizes of 1 × 5, 2 × 3, and 4 × 5 (Figs. S1–S3 in the online supplemental material). Smaller SOM sizes, i.e., 1 × 5 and 2 × 3, did not include patterns found in the larger SOMs and the transition between nodes was abrupt. The SOM method implicitly

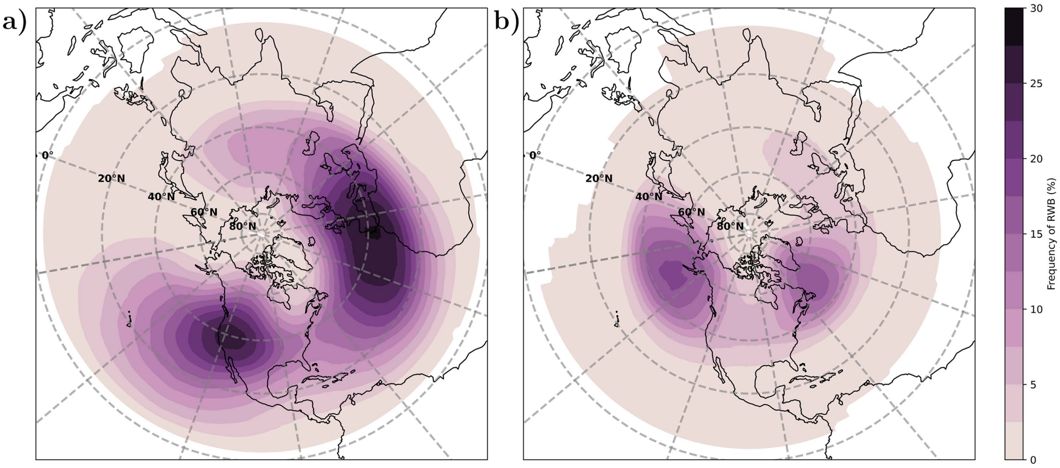

FIG. 2. Climatology of Northern Hemisphere (a) AWB and (b) CWB events during DJF from 1979 to 2019. The frequency (2.5% contour interval; colored) is presented as the percentage of time steps that wave breaking events were identified instantaneously at a given grid point. The meridians are plotted every 30° longitude.

assumes that the data exists on a continuum (Johnson et al. 2008), which is typically true for atmospheric variability. These abrupt transitions in the smaller SOMs are inconsistent with this assumption. Repetition of patterns was found in the larger 4 × 5 SOM. Therefore, the 3 × 4 SOM size was chosen as it allows for a simpler analysis with fewer nodes that still span the continuum of patterns in the input data. We also tested different values of the number of times each input data vector are provided per training, initial learning rates, and radii of influence, but well-constructed SOMs are less sensitive to these parameters (Gervais et al. 2016). The quality of the SOM was assessed using the quantization error, topological error, and Sammon map as in Gervais et al. (2016). The SOMs generated in this study were consistent with a well-constructed SOM since they had low quantization and topological errors, and a flat Sammon map (Fig. S4). For additional information on the SOM method, including user-defined parameters and quality metrics for SOM, the reader is referred to Kohonen (1982) and Gervais et al. (2016).

3. Results and discussion

a. *RWB climatology*

Climatologies of AWB and CWB were produced to ensure that wave breaking events were correctly identified in the ERA5 dataset. These climatologies, defined as the percentage of the overall time period that wave breaking events were identified at a given grid point, provide the geographical distribution of AWB and CWB events (Fig. 2). The AWB surf zones, or regions with frequent wave breaking events, were identified over the Pacific (~30°–50°N, 140°–100°W) and Atlantic (~25°–55°N, 50°W–30°E) basins and adjacent continents (Fig. 2a). These locations and frequencies match up well with surf zones shown in other studies (e.g., Strong and Magnusdottir 2008; Bowley et al. 2019a). Surf zones for CWB, 40°–60°N, 175°–145°W in the Pacific and 40°–60°N, 60°–30°W in the Atlantic (Fig. 2b), also match up well with prior work (Martius et al. 2007; Strong and Magnusdottir 2008; Bowley et al. 2019a). The Pacific basin has a higher frequency of CWB than the Atlantic during DJF which has also been shown in previous studies (Hitchman and Huesmann 2007; Strong and Davis 2007; Bowley et al. 2019a). The prevalence of CWB occurrence poleward relative to AWB is expected given that cyclonic (anticyclonic) shear is generated poleward (equatorward) of the jet. The similarity between the climatologies in this study and prior work confirm that the wave breaking identification algorithm is effectively identifying AWB and CWB events in the ERA5 dataset.

b. *SOM and associated tropopause fields of AWB and CWB events*

The AWB and CWB events identified in the ERA5 data were used to produce two SOMs: an AWB SOM and a CWB SOM (Fig. 3). The SOM nodes, or RWB flavors, are labeled using a $[x, y]$ convention according to their position in the SOM (e.g., the top-left node is node [1, 1] and the bottom-right node is [3, 4]). The BMU hit frequency, located in the top right corner of each node, is presented as a percentage of all RWB events that have been assigned to a given SOM node. These range from 6.7% to 9.6% in the AWB SOM and from 7.3% to 10.0% in the CWB SOM; thus, every node is associated with at least 900 wave break events. The resulting SOM of AWB and CWB demonstrate a range of flavors of RWB between events of the same type. The "flavor" terminology was first employed by Johnson (2013) and will refer here to the different patterns of RWB represented by each SOM node.

There are discernible differences of the magnitude of the potential temperature gradient ($|\nabla\theta|$) between the nodes for the AWB events in Fig. 3a. The $|\nabla\theta|$ on the poleward flank of the high θ streamer increases from the left side column to the right side of the AWB SOM. This region of enhanced $|\nabla\theta|$ appears to be strongly influenced by the position of a tropopause trough which is evident by the position of the lowest θ air in nodes on the right side of the AWB SOM (i.e., [1, 3], [2, 3], [3, 3], [1, 4], [2, 4], and [3, 4]). For nodes [1, 3] and [2, 3], the trough associated

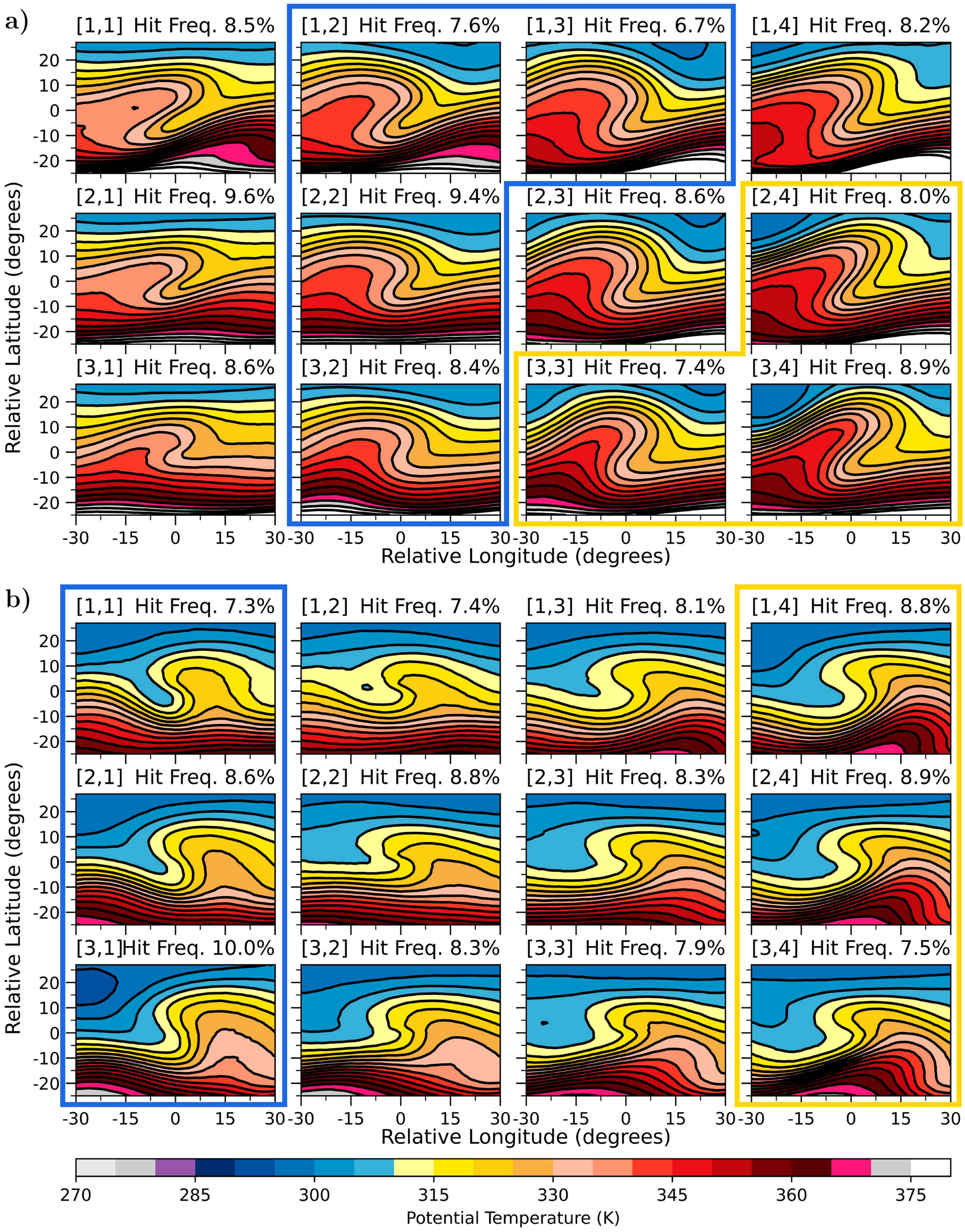

FIG. 3. The SOM of DT θ field (5-K contour interval; colored) for (a) AWB and (b) CWB events. The hit frequency is the percentage of the appearance of a given node in the entire SOM. The latitude and longitude (degrees) are relative to the RWB centroid. The blue and gold boxes in (a) represent the ridge-dominant nodes and strong poleward jet nodes, respectively, while the blue and gold boxes in (b) represent the omega block nodes and occlusion nodes, respectively.

with the low θ streamer (northeast region of the domain) leads to a more zonal orientation of the isentropes and slightly weaker $|\nabla\theta|$. This contrasts with nodes [2, 4] and [3, 4], where the deeper trough is upstream of the wave break (northwest region) resulting in a southwest–northeast tilt of the isentropes and a larger $|\nabla\theta|$. Similar processes appear to occur along the equatorward flank with the intrusion of higher θ air. The equatorward $|\nabla\theta|$ decreases from the top row to the bottom row of the AWB SOM. High θ air ($\geq$375 K) associated with a downstream ridge near 20°S and 0°–15°E is found along the top row. The largest $|\nabla\theta|$ in

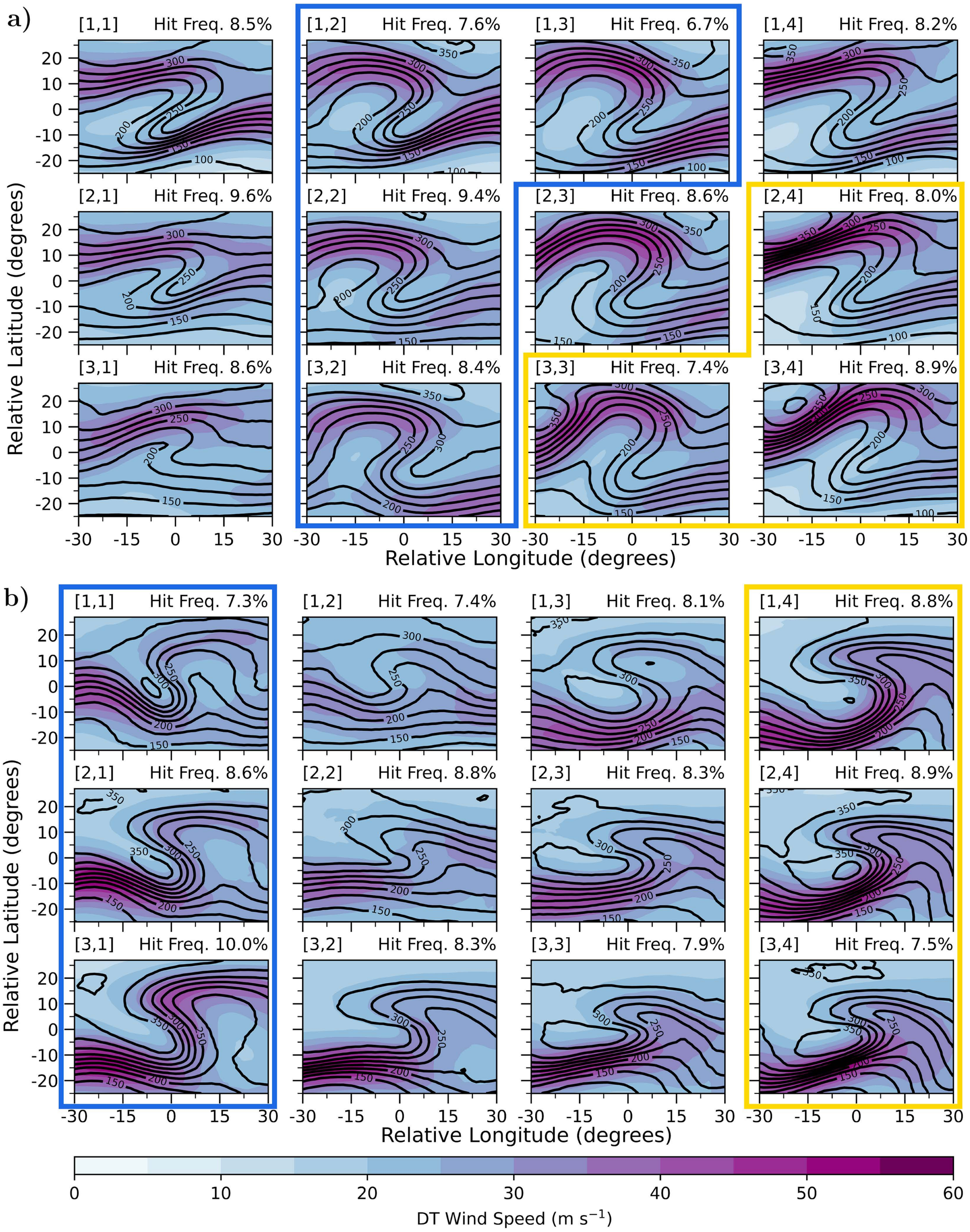

FIG. 4. The pressure (50-hPa interval; solid black contour) and wind speed (5 m s^{-1} interval, colored) on the dynamic tropopause for each node in the (a) AWB SOM and (b) CWB SOM. The hit frequencies, axes, and boxes are as described in Fig. 3.

the AWB SOM is observed in these nodes as a result. The downstream ridging also acts to align the isentropes from southwest to northeast in the equatorward portion of the wave break. Examination of the bottom row (i.e., [3, 1] to [3, 4]) reveals a more zonal pattern on the equatorward flank, with the highest θ air positioned near 20°S, 25°W aligned with the poleward intruding high θ streamer. Correspondingly, the equatorward $|\nabla\theta|$ is not as large and the isentropes are more oriented from west to east.

Composites of jet speed and direction on the DT are expected to vary across the SOM due to differences in $|\nabla\theta|$ and the orientation of the isentropes (Fig. 4a). Nodes with deeper tropopause troughs on the upstream (northwest) side of the AWB event ([1, 4], [2, 4], [3, 3] and [3, 4]) have a southwest–northeast-oriented poleward jet, while those with the deeper trough associated with the low θ streamer ([1, 2], [1, 3], and [2, 2], and [3, 2]) have a more zonally oriented poleward jet. Typically, a zonally oriented jet may be seen on the poleward flank of a block (e.g., Tyrlis and Hoskins 2008) which motivates us to label nodes [1, 2], [1, 3], [2, 2], and [3, 2] as the *ridge-dominant nodes* (outlined by the blue box in Fig. 3a) to facilitate discussion. Our lower-tropospheric composites will show that the ridge-dominant nodes are associated with a strong surface anticyclone. Nodes with troughs in both regions ([2, 3], [3, 3] and [3, 4]) have a more curved jet. The flavors with the most notable downstream ridging (top row) exhibit a stronger equatorward jet streak and are generally characterized by a double jet structure with jet streaks along the upstream and downstream flanks of the wave break. This is consistent with previous work which has shown a split jet structure along the poleward and equatorward flanks of an AWB (e.g., Strong and Magnusdottir 2008; Tamarin-Brodsky and Harnik 2023). Nodes [1, 4] and [2, 3] generally represent a smooth transition between the nodes with the strong poleward jet and strong equatorward jet as is expected given a continuum of patterns with SOM. Last, the poleward intrusion of the highest θ air in nodes [2, 4], [3, 3], and [3, 4] is generally associated with an enhanced $|\nabla\theta|$ near 10°N, 15°W. Correspondingly, a strong, narrow jet is present in these flavors on the poleward flank of the AWB. Therefore, we will refer to nodes [2, 4], [3, 3], and [3, 4] as the *strong poleward jet nodes* (gold outline; Fig. 3a).

There are also wave break events that are not characterized by strong jet structures. The speed of the jet on each flank of the wave break in nodes [2, 1] and [3, 1] is much weaker relative to the other nodes. In these nodes, the jet speed does not exceed 40 m s^{-1} throughout the extent of the wave break region. It will also be shown that these nodes have a much less amplified lower-tropospheric response. Therefore, we will limit the rest of the AWB flavor discussion to the strong poleward jet and ridge-dominant nodes as they have a larger tropospheric response resulting in robust surface weather impacts.

Notable differences between features on the DT were also found for the CWB flavors. The orientation of the ridge axis (high θ streamer) is remarkably different across the SOM (Fig. 3b). Nodes [1, 1], [2, 1], and [3, 1] resemble an omega block with a wide, neutrally tilted ridge, and we will subsequently refer to these as the *omega block nodes* (blue outline; Fig. 3b). These nodes also have an upstream ridge on the equatorward flank of the low θ streamer. The nodes on the right side of the SOM (i.e., nodes [1, 4], [2, 4], and [3, 4]) resemble a strongly tilted pattern, with a positively tilted ridge on the equatorward flank of the CWB becoming negatively tilted downstream of the low θ streamer. The alignment of the equatorward ridge with the low θ streamer shifts eastward from the left side of the SOM to the right, resulting in an increased $|\nabla\theta|$ and a transition from a northwest–southeast tilt of the isentropes to one more southwest–northeast. The trough shape (low θ streamer), especially evident by the location of low θ ($\leq$310 K) air, varies between sides of the SOM. The low θ impinges farther into the wave break center in the left SOM nodes whereas the low θ air is farther west on the right side of the SOM.

Jet speed increases from the top row to the bottom row and from left to right which is consistent with the increase in $|\nabla\theta|$ on the equatorward flank (Fig. 4b). Differences in the tilt of the jet on the equatorward flank of the low θ streamer between CWB flavors are notable. The omega block nodes are characterized by a northwest to southeast orientation of the jet streak, while the right side of the SOM (nodes [1, 4], [2, 4], and [3, 4]) exhibits a jet streak that is faster and aligned from southwest to northeast. The lower-tropospheric composites of these nodes will reveal features associated with occluded surface cyclone structures; thus nodes [1, 4], [2, 4], and [3, 4] will be referred to as the *occlusion nodes* (gold box; Fig. 3b). The omega block nodes also have a remarkable double jet streak structure, with a secondary jet streak located along the poleward flank of the high θ streamer that strengthens from the top row to the bottom row of the SOM. This appears to be in association with the highest tropopause heights (with pressures less than 200 hPa) in the high θ streamer (node [3, 1]) of any CWB flavor.

Evidence of transitional nodes are apparent with the middle two columns of the CWB flavors. Nodes [3, 2], and [3, 3] are transitional nodes between the bottom corners of the CWB SOM ([3, 1] and [3, 4]). Strong upstream jet streaks are present in nodes [3, 2] and [3, 3] but there is a weaker pressure gradient along the poleward flank of the wave break (Fig. 4b) resulting in weaker winds. Nodes [1, 2] and [1, 3] are additional examples of transitional nodes between the top left ([1, 1]) and top right ([1, 4]) nodes. The areal extent of higher wind velocities (>40 m s^{-1}) is minimal in these nodes due to weakening of $|\nabla\theta|$ on the southern flank of CWB in response to the positioning of the equatorward ridge. As would be expected with reduced jet-driven dynamical forcing, the sensible weather impacts are greatest in the omega block nodes and the occlusion nodes compared to the transition nodes. Therefore, we will focus the rest of our discussion on both of these subcategories of flavors.

c. *Tropospheric features associated with AWB flavors*

In this section, AWB SOM node composites of RWB events will be shown for a variety of tropospheric variables. This will provide information regarding the implications of the identified RWB flavors for the synoptic-scale flow. The influence of the jet structures discussed in the previous section on the midtroposphere can be understood by evaluating the 500-hPa height and relative vorticity field (Fig. 5a). The strong poleward jet nodes (gold box; Fig. 5a) have the largest cyclonic relative vorticity of all the nodes. The relative vorticity maxima in these nodes is located along the upstream trough near 15°N, 10°W. The orientation of the 500-hPa heights and relative vorticity imply large geostrophic, cyclonic relative vorticity advection (CVA) along the northern periphery of the high θ streamer in these nodes. Based on principles from quasigeostrophic theory, geostrophic CVA is expected to generate synoptic-scale ascent and this is evident in the 700-hPa vertical velocity (ω) field (Fig. 6a). For the strong poleward jet nodes, strong ascent of less than -2 dPa s^{-1} is present along the upstream flank of the wave break (Fig. 6a). This area of large, negative ω coincides with the area of large geostrophic CVA and is near the left exit region of a cyclonically curved jet streak. The line-like elongation of the ω field in these

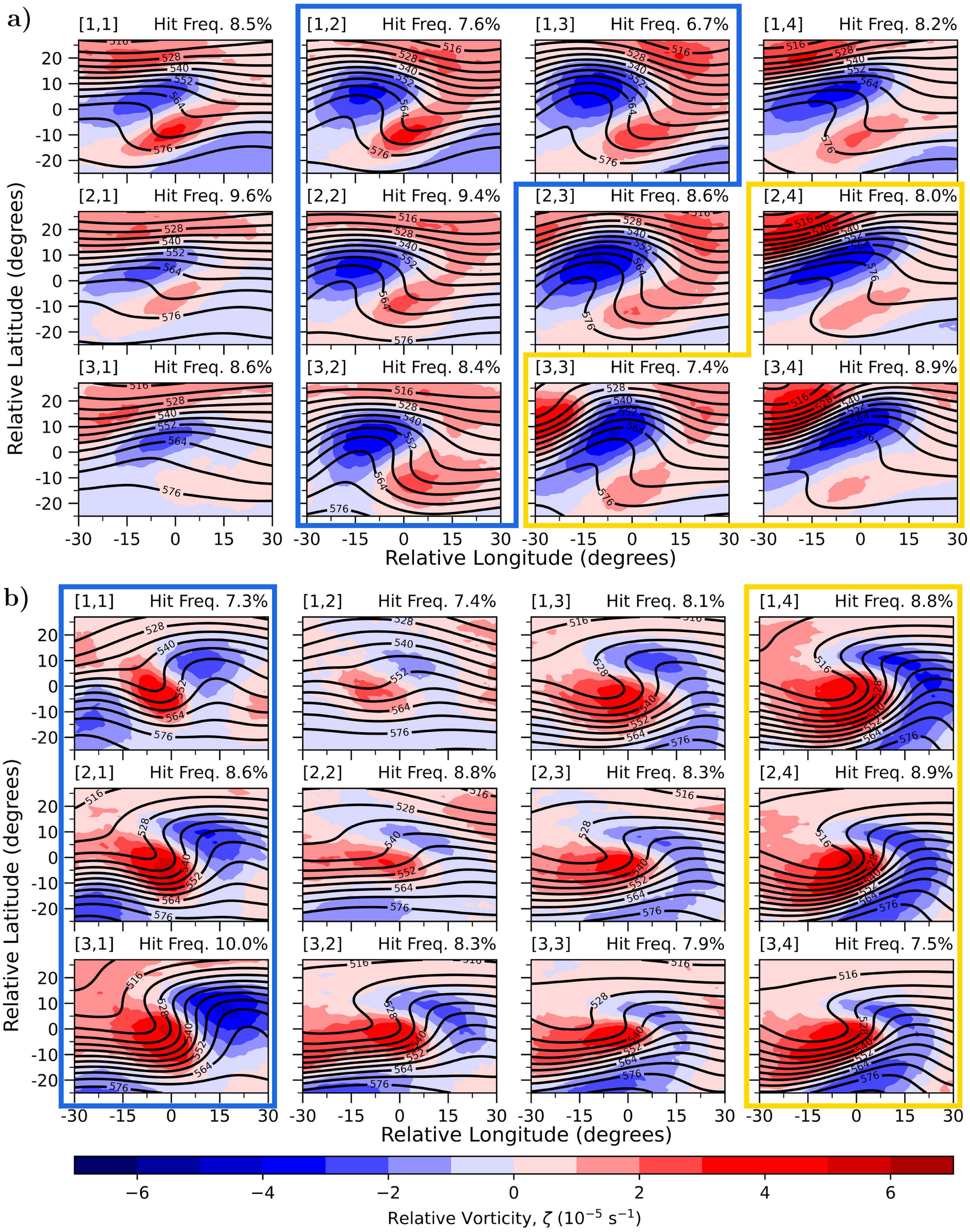

FIG. 5. The 500-hPa vorticity (1×10^{-5} s^{-1} interval; colored) and geopotential height (6-dm interval, solid black contour) fields for each of the (a) AWB and (b) CWB SOMs. The hit frequencies, axes, and boxes are as described in Fig. 3.

nodes is also likely indicative of lower-tropospheric fronts. The orientation of the 500-hPa heights and relative vorticity in the center and northeast quadrant of the strong poleward jet nodes are suggestive of a broad region of anticyclonic relative vorticity advection (AVA) oriented from southwest to northeast. Broad subsidence of 0.5–1 dPa s^{-1} is found downstream of the AWB event as expected in response to this AVA (Fig. 6a).

In the ridge-dominant nodes (blue box; Fig. 5a), the largest cyclonic relative vorticity is in the trough associated with the low θ streamer. This enhancement of cyclonic relative vorticity is likely due to the more closely aligned left exit and right entrance regions of the corresponding upstream and downstream jet streaks. The enhanced anticyclonic curvature in the upper-tropospheric heights in these nodes also result in a

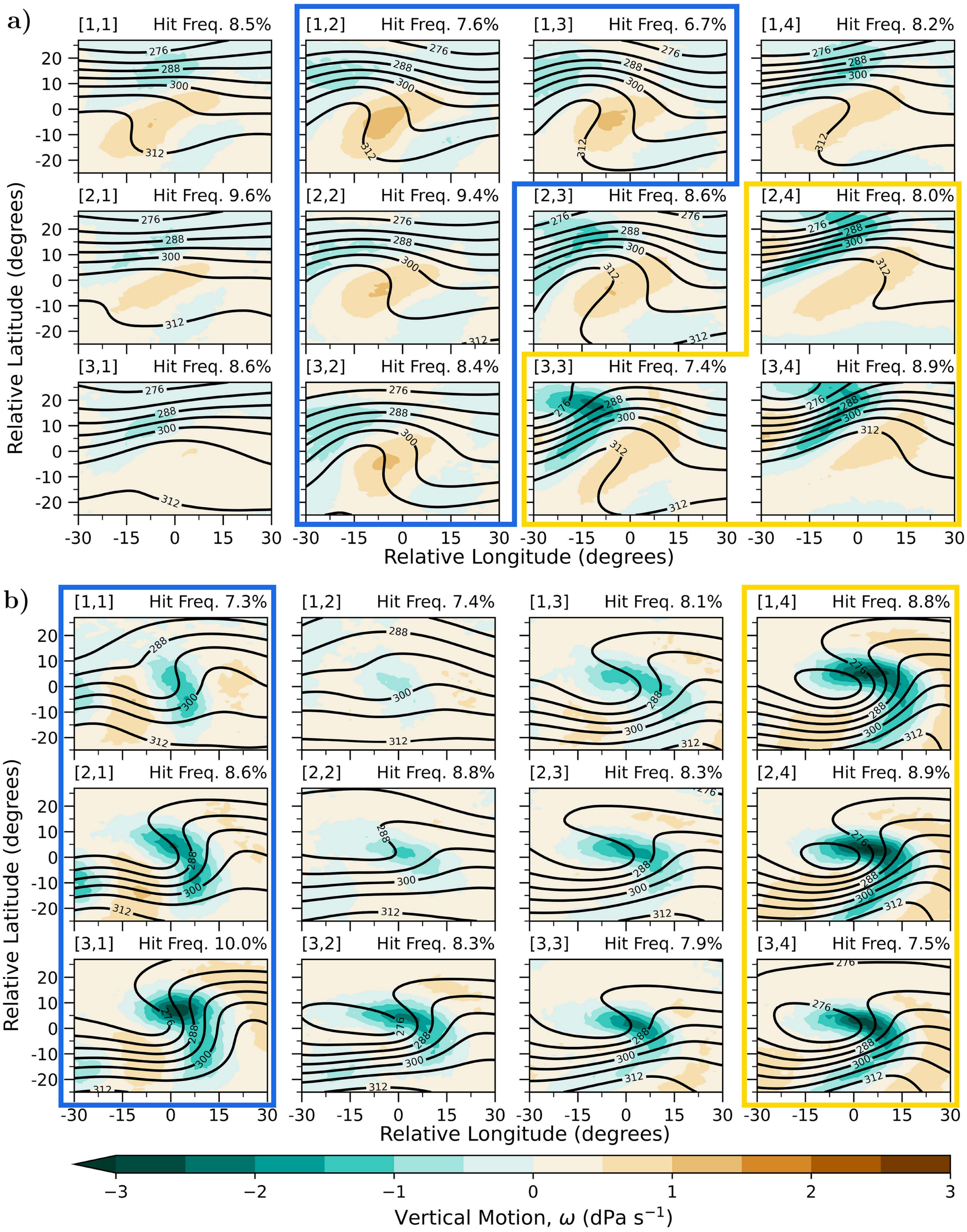

FIG. 6. The 700-hPa omega (0.5 dPa s^{-1} interval; colored) and geopotential height (6-dm interval, solid black contour) fields for each of the (a) AWB and (b) CWB SOMs. The hit frequencies, axes, and boxes are as described in Fig. 3.

more potent anticyclonic relative vorticity minima. Thus, the ridge-dominant nodes are expected to have a corridor of enhanced AVA oriented across the center of the wave break in response to this pattern. Correspondingly, the descending air in this region is stronger in the ridge-dominant nodes with ω between 1 and 1.5 dPa s^{-1} (Fig. 6a). There is also much less ascent along the upstream flank of these events compared to the strong jet nodes. Consequently, these nodes are associated with a more amplified 700-hPa ridge and strong (≥1024 hPa) and zonally elongated surface high pressure (Fig. 7a).

Next, we examine the moisture transport and precipitation fields associated with AWB. MSLP and IWVT fields are composited for each of these nodes in Fig. 7a. The IWVT was calculated in the ERA5 dataset as the flow rate (kg m^{-1} s^{-1})

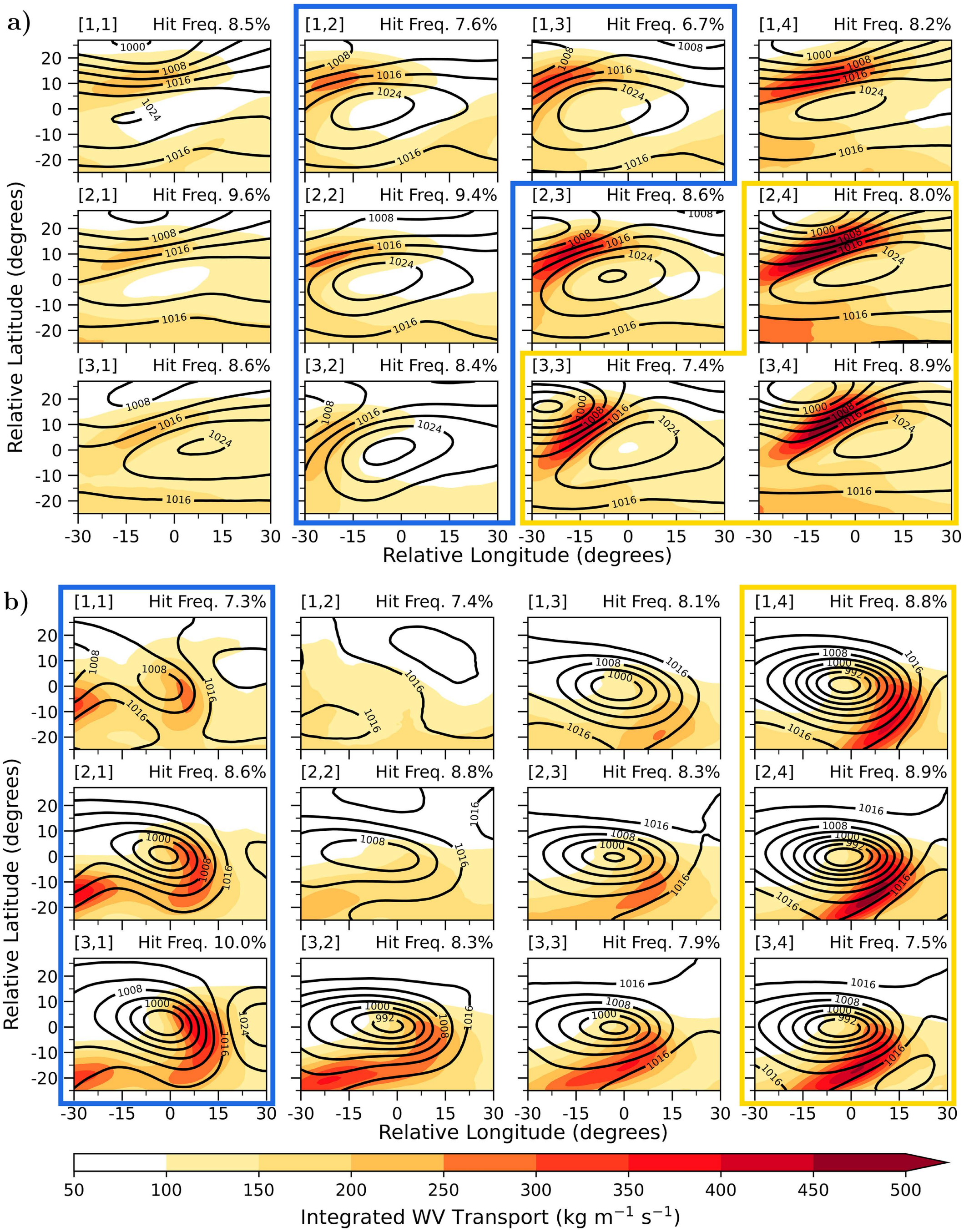

FIG. 7. The integrated water vapor transport (50 kg m^{-1} s^{-1} interval; colored) and mean sea level pressure fields (4-hPa interval; solid black contour) for each of the (a) AWB and (b) CWB SOMs. The hit frequencies, axes, and boxes are as described in Fig. 3.

of water vapor in a column extending from the surface to the top of the atmosphere. Analysis of IWVT and MSLP is useful as these variables can be used to diagnose influences on sensible weather features such as precipitation and the surface circulation. The strong poleward jet nodes are characterized by a deep (≤996 hPa) low pressure region upstream of the wave break (Fig. 7a). There is a large horizontal pressure gradient near 10°N and between 0° and 10°W in these nodes. This large surface pressure gradient is driven by the baroclinic development of the surface high from the AWB and coincides with the largest magnitude of IWVT. The MSLP pattern consisting of the upstream low and the strong anticyclone along the wave break is similar to MSLP anomaly patterns from the centered anticyclone composites of Tamarin-Brodsky and Harnik (2023) and the wave break centered composites of Strong and Magnusdottir (2008).

In the strong poleward jet nodes, the AWB generates a surface anticyclone that strongly contributes to channeling a narrow and potent stream of moisture poleward. IWVT values greater than 450 kg m^{-1} s^{-1} are present in two of the composites of the strong poleward jet nodes ([2, 4] and [3, 4]), which nearly meets the criteria for a moderate AR (≥500 kg m^{-1} s^{-1}) defined by Ralph et al. (2019). The composite of nodes [2, 4] and [3, 4] were created using 1738 and 1934 AWB events, respectively. The patterns of moisture transport in these AWB flavors are similar to the poleward IWVT patterns found by Liu and Barnes (2015) in the high latitudes of the eastern Atlantic. However, it should be noted that the composites represent events across all latitudes (i.e., poleward moisture transport does not guarantee Arctic moisture intrusion). A few of the IWVT patterns in the strong poleward jet nodes also resemble the IWVT fields associated with ARs and extreme precipitation in Norway (Michel et al. 2021). Node [3, 3] has a zonally thin channel of IWVT that extends southeast of the upstream cyclone. Michel et al. (2021) found that EPEs in western Norway were characterized by similar IWVT fields that were predominantly driven by AWB.

Heavy precipitation occurs in the strong poleward jet nodes as shown in Fig. 8a. Along the upstream flank of these nodes, the mean precipitation rate exceeds 10 mm day^{-1}. The location of the largest precipitation rates is coincident with the largest IWVT magnitudes (Fig. 7a) and the strongest forcing for ascent (Fig. 6a). This suggests these AWB events would be associated with synoptic-scale precipitation events along upstream flank of the event as seen in Bowley et al. (2019b). Additionally, it is useful to understand how RWB events are connected to episodes of extreme precipitation. To understand this relationship, we choose to define precipitation as extreme if the precipitation rate exceeds the 99th percentile at a given geographical location. For each RWB event, we identify RWB event-centered grid boxes that would be classified as extreme for their location. Then, we show the frequency of extreme events at each event-centered grid box in our RWB flavor composites. Along the upstream flank of the strong poleward jet nodes, 2.5%–7% of events in these flavors are considered extreme, which is far greater than the expected frequency of 1%. This implies that the strong poleward jet nodes play a role in EPEs.

In the ridge-dominant nodes, high surface pressure is positioned slightly west and across the center of the wave break, and the upstream low is displaced ≥30° longitude from the wave break center (Fig. 7a). The surface pressure gradient is weaker and isobars are oriented more zonally than in the strong poleward jet nodes. Given the background climatological water vapor gradient (pointed equatorward), this generates less effective moisture transport by the surface circulation. As a result, the IWVT and precipitation rates of these AWB events are much weaker than some of the other nodes (Figs. 7a and 8a). However, despite the reduced magnitudes of IWVT and precipitation rate, the ridge-dominant nodes can result in extreme precipitation. As many as 2.5% of events in these nodes are associated with extreme precipitation which is over twice the expected frequency (Fig. 8a). These results demonstrate a clear link between the synoptic-scale flow between nodes that are first elucidated by the SOM AWB flavors and precipitation and moisture transport patterns.

Another important aspect to consider is the geographical distribution of each node. In Fig. 9a, the frequency of occurrence is presented for each node similar to that for all events in Fig. 2. The sum of the frequency across all nodes will return the total frequency of RWB in Fig. 2. The climatology of the ridge-dominant nodes reveal notable differences between flavors. Nodes [1, 2] and [1, 3] largely occur across the west coast of the United States near 30°–45°N, 120°–90°W. The climatological planetary ridge in the Pacific is positioned along these longitudes during DJF. Therefore, AWB near this location enhances the climatological ridge along the U.S. West Coast as shown by Tyrlis and Hoskins (2008). Another distinguishable feature of the frequency for ridge-dominant nodes is seen in nodes [2, 2] and [3, 2]. The surf zones for these nodes appear to occur at higher latitudes (around 45°–55°N and along the prime meridian and near 120°W) than the climatology (Fig. 2a).

The frequency of occurrence for the strong poleward jet nodes reveals several notable features. The strong poleward jet nodes occur most frequently across the North Atlantic basin close to the climatological maximum in the area 20°–40°N, 60°–20°W (Figs. 2a and 9a). Greater than 50% of EPEs in this region were found to occur with an identified RWB and large IWVT structure, consistent with the composites of IWVT and precipitation in these nodes (de Vries 2021). Röthlisberger et al. (2016) further found that AWB across the North Atlantic basin coincides with anomalously large precipitation near 32°N, 15°W. However, the strong poleward jet events are not limited to the subtropical Atlantic basin as there are large values of frequency of occurrence across the west coast of the United States as well. It is notable that each of the surf zones for the strong poleward jet nodes are equatorward of the surf zones presented in Fig. 2a. Although these AWB events occur in regions with larger climatological water vapor concentrations, additional testing removing the zonal mean of IWVT for these events revealed similar structures of enhanced IWVT channels in the composites (Fig. S5).

d. *Tropospheric features associated with CWB flavors*

Similar to the AWB SOM, CWB event composites for each SOM node are computed to elucidate the tropospheric features associated with CWB flavors. Analysis of the 500-hPa relative vorticity and geopotential height reveal robust, poleward geostrophic CVA across the center of the CWB event in the omega block nodes (blue box; Fig. 5b). This implies a strong, synoptically forced ascent mechanism across the wave break center for these flavors which is confirmed in Fig. 6b. Ascent exceeding −2.5 dPa s^{-1} is found in nodes [2, 1] and [3, 1] and is oriented from north to south near 5°N, 5°E. Further ascent upstream of the wave break near 10°S, 30°W is also seen which may indicate trailing secondary cyclone development. This would be consistent with analysis of cyclone families by Pinto et al. (2014) who found that secondary upstream cyclogenesis occurs upstream of CWB along the cold front of a parent cyclone. In that study, the parent and secondary low form near the left exit and right entrance regions of the jet, respectively, which is especially apparent in node [3, 1] (Fig. 4b).

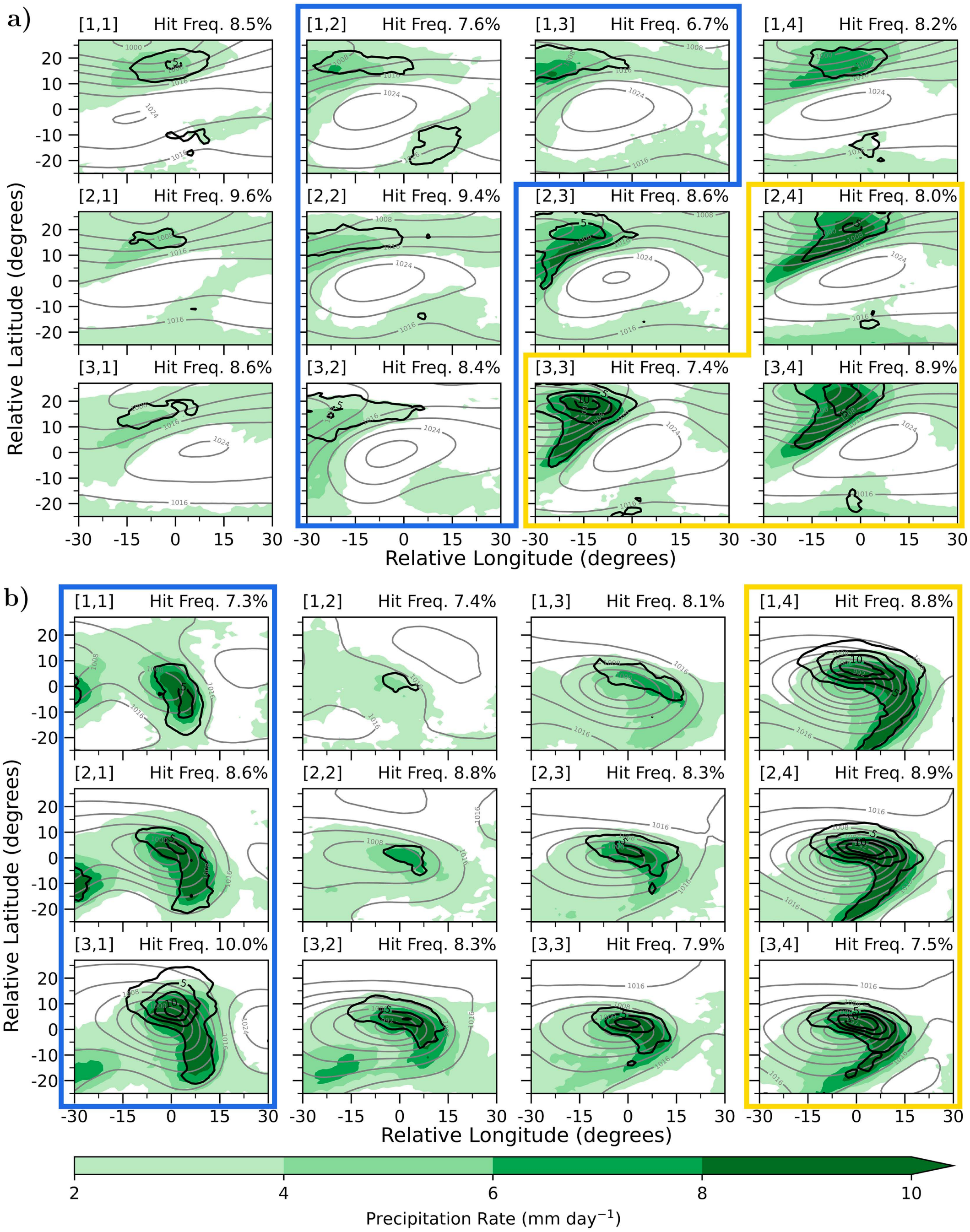

FIG. 8. The mean total precipitation rate (2 mm day^{-1} interval; colored), mean sea level pressure (4-hPa interval; thin gray contour), and the frequency of extreme precipitation (defined as exceedance of the 99th percentile) for daily precipitation rate at a given grid point (2.5% interval starting at 2.5%; solid black contour) for each of the (a) AWB and (b) CWB SOMs. The hit frequencies, axes, and boxes are as described in Fig. 3.

There is also a large area of high-magnitude anticyclonic relative vorticity in these nodes which extends nearly 20° of longitude downstream of the wave break. As a result, there is a broad area of weak (~0.5 dPa s^{-1}) subsidence near 10°N, 15°E. The midtropospheric ridge in these nodes covers nearly 30° of latitude downstream of the CWB.

The magnitudes of cyclonic relative vorticity are comparable between the omega block and occlusion nodes, yet the orientation of the geopotential height fields are notably different. The ridge and associated narrow region of anticyclonic relative vorticity is bent back to ~15°N, 5°W in the occlusion nodes (Fig. 5b). This, coupled with a broad region of cyclonic vorticity associated

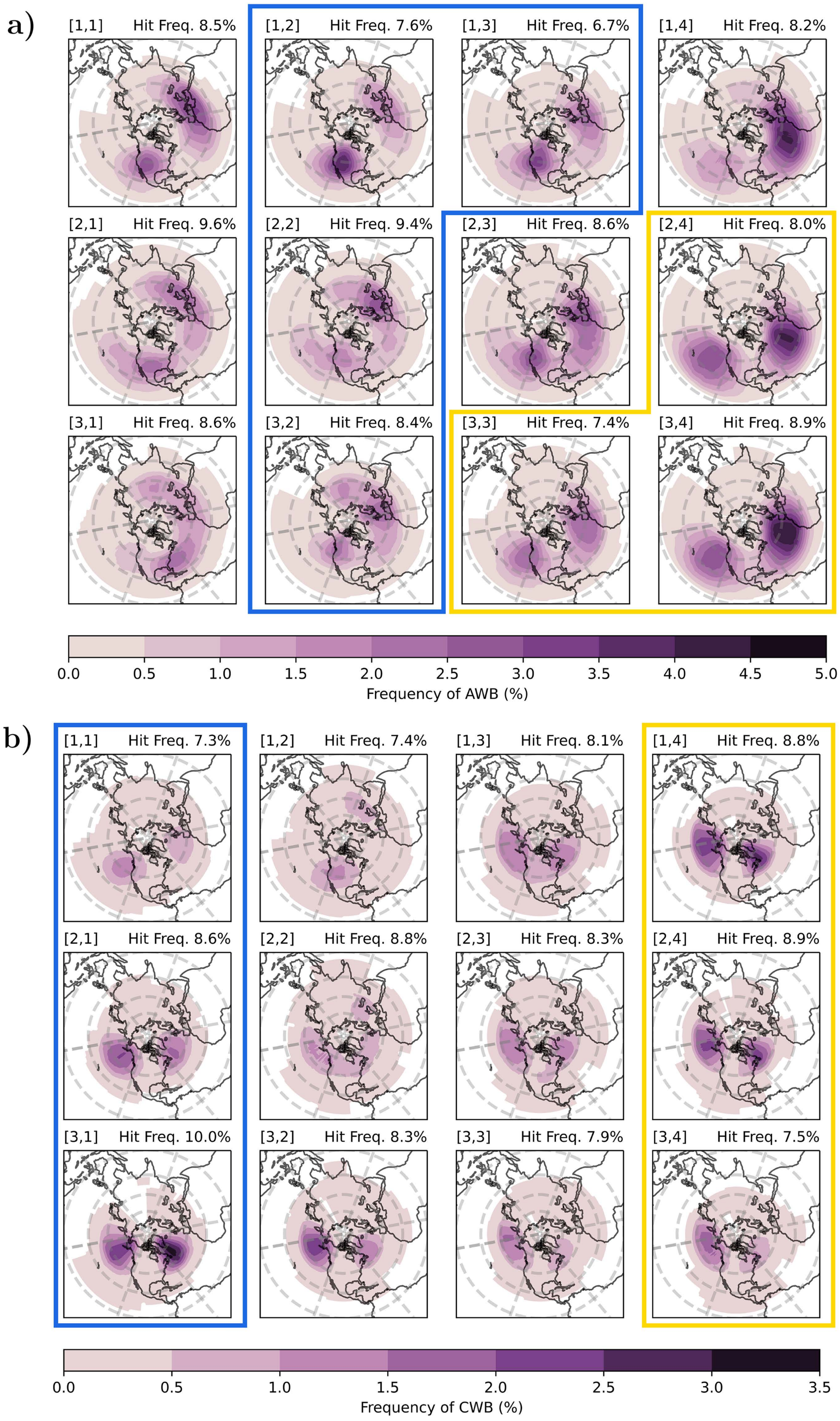

FIG. 9. Frequency of occurrence of (a) AWB and (b) CWB events during DJF from 1979 to 2019 by node. The frequency (0.5% contour interval; colored) is the percentage of time steps that wave breaking events were identified instantaneously at a given grid point for each node. The meridians are plotted every 60° longitude and the parallels are plotted every 20° latitude starting at the equator.

with the high θ streamer, results in vigorous geostrophic CVA from the center of the wave break into the apex of the poleward intruding ridge. Correspondingly, large synoptic-scale ascent exceeding -2.5 dPa s^{-1} is found in this region (Figs. 5b and 6b). The ascent in the occlusion nodes has the largest magnitude and areal extent of the CWB SOM. These midlevel structures suggest that the surface cyclone is late in its life cycle since the midlevel trough is negatively tilted with closed 700-hPa height contours vertically stacked beneath the 500-hPa trough. The region of largest ascent is longitudinally elongated and resembles the shape of a comma head. Often, the comma head cloud pattern is associated with mature midlatitude cyclones (Henry 1922; Carlson 1980). Both points of evidence are suggestive of a surface cyclone that is late in its life cycle and occluded. Geostrophic AVA is evident downstream of the ridge, resulting in a broad area of subsidence that extends ≥15° of longitude and the development of a surface high near ~20°S, 25°E (Fig. 7b).

The MSLP field exemplifies a troposphere deep response to CWB (Fig. 7b) in both subcategories of CWB events. Notably, the position of the surface cyclone along the wave break center is in a very similar location to what was found in the cyclone centered composites of Tamarin-Brodsky and Harnik (2023) as well as the wave break centered composites of Strong and Magnusdottir (2008). Omega block nodes [2, 1] and [3, 1] have deep surface low pressure (≤996 hPa) and a strong (≥1020 hPa) downstream surface high. A north–south channel of moderately high (≥350 kg m^{-1} s^{-1}) IWVT and precipitation rates (≥10 mm day^{-1}) are seen in these nodes (Figs. 7b and 8b) which appears to aid in generating precipitation extremes. Between 5% and 10% of CWB events for each flavor in the omega block nodes are linked to extreme precipitation. There are two surface features that appear to drive these localized IWVT and precipitation maxima. The first feature is the surface cyclone and anticyclone located in the area 0°–15°S, 0°–30°E (Figs. 5b and 7b). The largest surface pressure gradient in the omega block nodes is positioned between 10° and 15°E of the CWB center. Therefore, strong surface winds, generated from the large pressure gradient, are collocated with the maxima in IWVT. The second feature is the upstream surface high near 15°S, 15°W. Subsidence associated with this high pressure (Fig. 6b) acts to reduce moisture transport in this region. Another IWVT maxima is located 25°W of the center in the omega block patterns. This maxima further indicates that upstream cyclone development may be occurring in these flavors. This signal of extreme high moisture transport in these nodes is very similar to the central Pacific and east Atlantic CWB cases in Liu and Barnes (2015). The IWVT fields in nodes [2, 1] and [3, 1] also resemble the IWVT fields associated with EPEs in northern inland Norway that are primarily driven by CWB (Michel et al. 2021).

Amplified MSLP and IWVT patterns are also present in the occlusion nodes (Fig. 7b). The deepest surface low pressure systems (≤992 hPa) of the SOM are in these three nodes. Pressures of this magnitude are typically associated with strong, mature cyclones. The corridor of largest IWVT is oriented southwest to northeast and with values exceeding 400 kg m^{-1} s^{-1} across the downstream flank. IWVT values of this magnitude can be categorized as a weak AR event (Ralph et al. 2019). Precipitation rates exceed 10 mm day^{-1} along the channel of high IWVT, which extends 15°E of the wave break center and is collocated with regions of upward vertical velocity (Fig. 6). It is notable that as many as 5%–10% of CWB events for each of the occlusion nodes are associated with extreme precipitation near the surface cyclone (Fig. 8b). The moisture transport patterns in the occlusion nodes are less meridional compared to the omega block nodes. The position of the downstream surface high pressure is near 20°S, 15°E, which is farther south than the omega block nodes (Fig. 7b). The downstream ridge in the occlusion nodes closely matches the downstream anticyclone captured in the CWB MSLP anomaly fields of Tamarin-Brodsky and Harnik (2023). Furthermore, the upstream surface high is well southwest of the wave break center, limiting the subsidence-induced drying near the center of the CWB event (Fig. 6b). Correspondingly, the largest pressure gradient is positioned southeast of the center of the wave break which generates southwesterly surface flow and moisture transport in these CWB flavors (Fig. 5b). Therefore, the position of the downstream and upstream surface high relative to the attendant surface low appears crucial to dictating the orientation of the IWVT and precipitation fields between different flavors of CWB.

The omega block nodes, which make up about 25% of all CWB events (~3250 events), are located along the Pacific and Atlantic climatological storm tracks (Fig. 9b). The surf zones for these nodes are positioned between 40°–60°N, 170°–120°W in the Pacific and 40°–60°N, 60°–20°W in the Atlantic. The Atlantic basin CWB surf zone maxima in node [3, 1] is in a nearly identical location to blocking events examined by Tyrlis and Hoskins (2008) on the DT (Fig. 9b). Tyrlis and Hoskins (2008) labeled events similar to node [3, 1] as "hybrid" events where there are both anticyclonic and cyclonic developments. The MSLP fields are consistent with this idea since there is deep low pressure at the center of the wave break and strong high pressure downstream of the wave break. CWB in node [3, 1] occurs largely in the high latitudes (≥60°N), especially over the southern edge of Greenland. In the blocking weather regime discussed by Michel and Rivière (2011), a maxima in CWB was identified across a similar region as node [3, 1] extending between the south of Greenland and Iceland. CWB in this location was linked to the S-shaped part of an Ω-like structure (Michel and Rivière 2011). The IWVT and precipitation rate fields in the omega block nodes are oriented north–south, which is nearly identical to case studies presented in Liu and Barnes (2015). This, combined with their preferred regions of occurrence, implies that these flavors of CWB are crucial to extreme high moisture transport into the Arctic and high latitudes (e.g., Woods et al. 2013; Liu and Barnes 2015). The surf zones of the occlusion nodes are shifted slightly northwest of the omega block nodes and the climatological CWB surf zone (Fig. 2). Similar to the omega block patterns, the occlusion nodes make up about 25% of all CWB events. Thus, it is evident that between the occlusion and omega block nodes, a substantial portion (~6410 events) of CWB are linked to significant and impactful surface weather events.

4. Conclusions

The primary goal of this study was to determine how RWB events vary within the same type (e.g., AWB or CWB) by examining the synoptic-scale thermodynamic and dynamic fields throughout the troposphere. A RWB identification method from Bowley et al. (2019a) was used to identify instantaneous RWB events on the DT in the ERA5 dataset during winter for 6-hourly data over the 1979–2019 period. Using the latitude and longitude centroid of each event, 50° × 60° fields of θ^* on the DT were constructed for each identified wave break event. These DT θ^* fields were provided to a SOM algorithm that clustered wave break events into archetypal patterns, or flavors. This analysis revealed key distinctions in the shape of overturning isentropes between RWB events of the same type as well as notably strong signals in MSLP, IWVT, and precipitation that varied among different flavors of RWB events. To the authors' knowledge, this is the first attempt at classifying wave break types within the AWB/CWB framework.

The AWB SOM was characterized by differences in the magnitude of the meridional gradient in potential temperature across the map nodes. There are a suite of tropospheric features associated with different AWB flavors. A zonally elongated high developed in response to AWB in nodes [1, 2], [2, 2], [1, 3], and [3, 2] and we labeled these nodes as the ridge-dominant nodes. These flavors had stronger subsidence favoring the development of surface high pressure across the center of the wave break limiting the downstream propagation of the upstream surface cyclone. We labeled another subset of nodes as the strong poleward jet nodes (nodes [2, 4], [3, 3], and [3, 4]) and these flavors involved robust poleward moisture transport along the upstream flank of the AWB. Strong synoptic-scale forcing for ascent was present along the corridor of enhanced IWVT resulting in mean total precipitation rates exceeding 10 mm day^{-1}. Between 2.5% and 5% of AWB events in the strong poleward jet nodes were found to result in extreme precipitation.

CWB events were distinguished by the orientation of the isentropes and gradient in potential temperature on the upstream flank of the wave break. Although there are a range of CWB flavors, two subcategories of these nodes (six total) are associated with distinct and robust tropospheric impacts. The first, which we have labeled as the omega block nodes, closely resembled Atlantic blocking found by Tyrlis and Hoskins (2008) and were associated with a north–south corridor of IWVT exceeding 350 kg m^{-1} s^{-1} and precipitation rates exceeding 10 mm day^{-1}. These nodes frequently occurred north of 60°N, signifying the importance of CWB to moisture transport into the Arctic. The second subcategory, the occlusion nodes, are associated with deep surface low pressure less than 996 hPa across the center of CWB events. Similar to the omega block nodes, there were localized areas of high IWVT and precipitation rates exceeding 10 mm day^{-1}, but for the occlusion nodes these maxima were farther south of the center of the wave break. These precipitation rates were found to result in an increased frequency of extreme precipitation as 5%–10% of CWB events in each subcategory were associated with extreme precipitation (Fig. 8b). Although these CWB events occur in similar locations, they have vastly different sensible weather features. Therefore, RWB flavor appears to impact the type, location, and severity of tropospheric impacts.

In this study, 6-hourly time steps for each event were used as input data into the SOM. However, it is possible that some nodes are associated with earlier or later stages of RWB event life cycle. An intriguing question therefore remains as to how RWB event life cycles are being captured across the SOM nodes. To address this question, a tracking scheme would need to be applied to identify RWB events. Identification of preferred pathways through the SOM could then be used to assess potential predictability (Gu and Gervais 2021). However, this is outside the scope of this study.

Given the association between RWB and intense moisture transport, understanding how climate models represent RWB events is critical for assessing future changes in extreme hydrological events. Changes in the eddy-driven jet (speed and position) are expected due to climate change (e.g., Woollings and Blackburn 2012). This is of particular importance for RWB, which has been shown to be sensitive to jet structure (Thorncroft et al. 1993; Nakamura and Plumb 1994). Conducting the same SOM analysis using both ERA5 and climate model output (e.g., CESM-LENS2) can facilitate comparison between their respective RWB flavors and associated mechanisms. For example, a process-oriented climate model evaluation could be conducted to identify sources of model bias by comparing the differences in mechanisms governing sensible weather impacts from RWB events between the datasets. This would allow for further understanding of the source of climate model errors. Identifying RWB events in future climate model simulations can also allow for an investigation into projected changes of RWB events and their associated extreme weather impacts.

Acknowledgments. The authors thank Dr. Steve Feldstein, Dr. Colin Zarzycki, and three anonymous reviewers for providing constructive feedback that significantly improved this manuscript. Computations for this research were conducted using supercomputing resources provided by the National Center for Atmospheric Research (NCAR) Casper Computing Cluster and resources from The Pennsylvania State University Institute for Computational and Data Sciences (ICDS). This content is solely the responsibility of the authors and does not necessarily represent the views of the ICDS. This work has been supported by the National Science Foundation (AGS—Climate and Large-Scale Dynamics 2148567).

Data availability statement. ERA5 data are made available by the ECMWF through the Copernicus data storage system at doi:10.24381/cds.adbb2d47 and doi:10.24381/cds.bd0915c6. Derived DT fields from the ERA5 dataset, identified Rossby wave breaks, and self-organizing map output created for this study are openly available from the Penn State DataCommons at https://doi.org/10.26208/GA3Y-XD59. The Self-Organizing Map Program Package (SOM_PAK; Kohonen 1982) is available at http://www.cis.hut.fi/research/som-research/. Modifications of SOM_PAK conducted by Gu and Gervais (2022) to enable large input data vectors are outlined on Zenodo at https://doi.org/10.5281/zenodo.6416159.

REFERENCES

Abatzoglou, J. T., and G. Magnusdottir, 2006: Planetary wave breaking and nonlinear reflection: Seasonal cycle and interannual variability. *J. Climate*, **19**, 6139–6152, https://doi.org/10.1175/JCLI3968.1.

Appenzeller, C., H. C. Davies, and W. A. Norton, 1996: Fragmentation of stratospheric intrusions. *J. Geophys. Res.*, **101**, 1435–1456, https://doi.org/10.1029/95JD02674.

Barnes, E. A., and D. L. Hartmann, 2012: Detection of Rossby wave breaking and its response to shifts of the midlatitude jet with climate change. *J. Geophys. Res.*, **117**, D09117, https://doi.org/10.1029/2012JD017469.

Benedict, J. J., S. Lee, and S. B. Feldstein, 2004: Synoptic view of the North Atlantic Oscillation. *J. Atmos. Sci.*, **61**, 121–144, https://doi.org/10.1175/1520-0469(2004)061<0121:SVOTNA>2.0.CO;2.

Bowley, K. A., J. R. Gyakum, and E. H. Atallah, 2019a: A new perspective toward cataloging Northern Hemisphere Rossby wave breaking on the dynamic tropopause. *Mon. Wea. Rev.*, **147**, 409–431, https://doi.org/10.1175/MWR-D-18-0131.1.

——, ——, and ——, 2019b: The role of dynamic tropopause Rossby wave breaking for synoptic-scale buildups in Northern Hemisphere zonal available potential energy. *Mon. Wea. Rev.*, **147**, 433–455, https://doi.org/10.1175/MWR-D-18-0143.1.

Carlson, T. N., 1980: Airflow through midlatitude cyclones and the comma cloud pattern. *Mon. Wea. Rev.*, **108**, 1498–1509, https://doi.org/10.1175/1520-0493(1980)108<1498:ATMCAT>2.0.CO;2.

Cassano, E. N., A. H. Lynch, J. J. Cassano, and M. R. Koslow, 2006: Classification of synoptic patterns in the western Arctic associated with extreme events at Barrow, Alaska, USA. *Climate Res.*, **30**, 83–97, https://doi.org/10.3354/cr030083.

Cavazos, T., 2000: Using self-organizing maps to investigate extreme climate events: An application to wintertime precipitation in the Balkans. *J. Climate*, **13**, 1718–1732, https://doi.org/10.1175/1520-0442(2000)013<1718:USOMTI>2.0.CO;2.

de Vries, A. J., 2021: A global climatological perspective on the importance of Rossby wave breaking and intense moisture transport for extreme precipitation events. *Wea. Climate Dyn.*, **2**, 129–161, https://doi.org/10.5194/wcd-2-129-2021.

Dhital, S., M. L. Kaplan, J. A. G. Orza, and S. Fiedler, 2020: Atmospheric dynamics of a Saharan dust outbreak over Mindelo, Cape Verde Islands, preceded by Rossby wave breaking: Multiscale observational analyses and simulations. *J. Geophys. Res. Atmos.*, **125**, e2020JD032975, https://doi.org/10.1029/2020JD032975.

Gervais, M., E. Atallah, J. R. Gyakum, and L. B. Tremblay, 2016: Arctic air masses in a warming world. *J. Climate*, **29**, 2359–2373, https://doi.org/10.1175/JCLI-D-15-0499.1.

——, J. Shaman, and Y. Kushnir, 2019: Impacts of the North Atlantic warming hole in future climate projections: Mean atmospheric circulation and the North Atlantic jet. *J. Climate*, **32**, 2673–2689, https://doi.org/10.1175/JCLI-D-18-0647.1.

Gu, Q., and M. Gervais, 2021: Exploring North Atlantic and North Pacific decadal climate prediction using self-organizing maps. *J. Climate*, **34**, 123–141, https://doi.org/10.1175/JCLI-D-20-0017.1.

——, and ——, 2022: Diagnosing two-way coupling in decadal North Atlantic SST variability using time-evolving self-organizing maps. *Geophys. Res. Lett.*, **49**, e2021GL096560, https://doi.org/10.1029/2021GL096560.

Henry, A. J., 1922: J. Bjerknes and H. Solberg on life cycle of cyclones and the polar front theory of atmospheric circulation. *Mon. Wea. Rev.*, **50**, 468–473, https://doi.org/10.1175/1520-0493(1922)50<468:JBAHSO>2.0.CO;2.

Hersbach, H., and Coauthors, 2018: ERA5 hourly data on pressure levels from 1940 to present. Copernicus Climate Change Service (C3S) Climate Data Store (CDS), https://doi.org/10.24381/cds.bd0915c6.

Hewitson, B. C., and R. G. Crane, 2002: Self-organizing maps: Applications to synoptic climatology. *Climate Res.*, **22**, 13–26, https://doi.org/10.3354/cr022013.

Hitchman, M. H., and A. S. Huesmann, 2007: A seasonal climatology of Rossby wave breaking in the 320–2000-K layer. *J. Atmos. Sci.*, **64**, 1922–1940, https://doi.org/10.1175/JAS3927.1.

Hoskins, B. J., M. E. Mcintyre, and A. W. Robertson, 1985: On the use and significance of isentropic potential vorticity maps. *Quart. J. Roy. Meteor. Soc.*, **111**, 877–946, https://doi.org/10.1002/qj.49711147002.

Hu, H., F. Dominguez, Z. Wang, D. A. Lavers, G. Zhang, and F. M. Ralph, 2017: Linking atmospheric river hydrological impacts on the U.S. West Coast to Rossby wave breaking. *J. Climate*, **30**, 3381–3399, https://doi.org/10.1175/JCLI-D-16-0386.1.

Johnson, N. C., 2013: How many ENSO flavors can we distinguish? *J. Climate*, **26**, 4816–4827, https://doi.org/10.1175/JCLI-D-12-00649.1.

——, S. B. Feldstein, and B. Tremblay, 2008: The continuum of Northern Hemisphere teleconnection patterns and a description of the NAO shift with the use of self-organizing maps. *J. Climate*, **21**, 6354–6371, https://doi.org/10.1175/2008JCLI2380.1.

Kohonen, T., 1982: Self-organized formation of topologically correct feature maps. *Biol. Cybern.*, **43**, 59–69, https://doi.org/10.1007/BF00337288.

Liu, C., and E. A. Barnes, 2015: Extreme moisture transport into the Arctic linked to Rossby wave breaking. *J. Geophys. Res. Atmos.*, **120**, 3774–3788, https://doi.org/10.1002/2014JD022796.

——, X. Ren, and X. Yang, 2014: Mean flow–storm track relationship and Rossby wave breaking in two types of El-Niño. *Adv. Atmos. Sci.*, **31**, 197–210, https://doi.org/10.1007/s00376-013-2297-7.

Liu, Y., R. H. Weisberg, and C. N. K. Mooers, 2006: Performance evaluation of the self-organizing map for feature extraction. *J. Geophys. Res.*, **111**, C05018, https://doi.org/10.1029/2005JC003117.

Madsen, M. M., and J. E. Martin, 2023: A self-organizing maps analysis of wintertime North Pacific jet stream variability. *J. Climate*, **36**, 1863–1879, https://doi.org/10.1175/JCLI-D-22-0452.1.

Martius, O., C. Schwierz, and H. C. Davies, 2007: Breaking waves at the tropopause in the wintertime Northern Hemisphere: Climatological analyses of the orientation and the theoretical LC1/2 classification. *J. Atmos. Sci.*, **64**, 2576–2592, https://doi.org/10.1175/JAS3977.1.

Masato, G., B. J. Hoskins, and T. J. Woollings, 2012: Wave-breaking characteristics of midlatitude blocking. *Quart. J. Roy. Meteor. Soc.*, **138**, 1285–1296, https://doi.org/10.1002/qj.990.

McIntyre, M. E., and T. N. Palmer, 1983: Breaking planetary waves in the stratosphere. *Nature*, **305**, 593–600, https://doi.org/10.1038/305593a0.

Michel, C., and G. Rivière, 2011: The link between Rossby wave breakings and weather regime transitions. *J. Atmos. Sci.*, **68**, 1730–1748, https://doi.org/10.1175/2011JAS3635.1.

——, A. Sorteberg, S. Eckhardt, C. Weijenborg, A. Stohl, and M. Cassiani, 2021: Characterization of the atmospheric environment during extreme precipitation events associated with atmospheric rivers in Norway—Seasonal and regional aspects. *Wea. Climate Extremes*, **34**, 100370, https://doi.org/10.1016/j.wace.2021.100370.

Nakamura, M., and R. A. Plumb, 1994: The effects of flow asymmetry on the direction of Rossby wave breaking. *J. Atmos. Sci.*, **51**, 2031–2045, https://doi.org/10.1175/1520-0469(1994)051<2031:TEOFAO>2.0.CO;2.

Papin, P. P., L. F. Bosart, and R. D. Torn, 2020: A feature-based approach to classifying summertime potential vorticity streamers linked to Rossby wave breaking in the North Atlantic basin. *J. Climate*, **33**, 5953–5969, https://doi.org/10.1175/JCLI-D-19-0812.1.

Peters, D., and D. W. Waugh, 1996: Influence of barotropic shear on the poleward advection of upper-tropospheric air. *J. Atmos. Sci.*, **53**, 3013–3031, https://doi.org/10.1175/1520-0469(1996)053<3013:IOBSOT>2.0.CO;2.

Pinto, J. G., I. Gómara, G. Masato, H. F. Dacre, T. Woollings, and R. Caballero, 2014: Large-scale dynamics associated with clustering of extratropical cyclones affecting western Europe. *J. Geophys. Res. Atmos.*, **119**, 13 704–13 719, https://doi.org/10.1002/2014JD022305.

Polvani, L. M., and R. A. Plumb, 1992: Rossby wave breaking, microbreaking, filamentation, and secondary vortex formation: The dynamics of a perturbed vortex. *J. Atmos. Sci.*, **49**, 462–476, https://doi.org/10.1175/1520-0469(1992)049<0462:RWBMFA>2.0.CO;2.

Postel, G. A., and M. H. Hitchman, 1999: A climatology of Rossby wave breaking along the subtropical tropopause. *J. Atmos. Sci.*, **56**, 359–373, https://doi.org/10.1175/1520-0469(1999)056<0359:ACORWB>2.0.CO;2.

Ralph, F. M., J. J. Rutz, J. M. Cordeira, M. Dettinger, M. Anderson, D. Reynolds, L. J. Schick, and C. Smallcomb, 2019: A scale to characterize the strength and impacts of atmospheric rivers. *Bull. Amer. Meteor. Soc.*, **100**, 269–289, https://doi.org/10.1175/BAMS-D-18-0023.1.

Rivière, G., 2009: Effect of latitudinal variations in low-level baroclinicity on eddy life cycles and upper-tropospheric wave-breaking processes. *J. Atmos. Sci.*, **66**, 1569–1592, https://doi.org/10.1175/2008JAS2919.1.

Rodgers, K. B., and Coauthors, 2021: Ubiquity of human-induced changes in climate variability. *Earth Syst. Dyn.*, **12**, 1393–1411, https://doi.org/10.5194/esd-12-1393-2021.

Röthlisberger, M., S. Pfahl, and O. Martius, 2016: Regional-scale jet waviness modulates the occurrence of midlatitude weather extremes. *Geophys. Res. Lett.*, **43**, 10 989–10 997, https://doi.org/10.1002/2016GL070944.

——, L. Frossard, L. F. Bosart, D. Keyser, and O. Martius, 2019: Recurrent synoptic-scale Rossby wave patterns and their effect on the persistence of cold and hot spells. *J. Climate*, **32**, 3207–3226, https://doi.org/10.1175/JCLI-D-18-0664.1.

Schuenemann, K. C., and J. J. Cassano, 2010: Changes in synoptic weather patterns and Greenland precipitation in the 20th and 21st centuries: 2. Analysis of 21st century atmospheric changes using self-organizing maps. *J. Geophys. Res.*, **115**, D05108, https://doi.org/10.1029/2009JD011706.

Strong, C., and R. E. Davis, 2007: Winter jet stream trends over the Northern Hemisphere. *Quart. J. Roy. Meteor. Soc.*, **133**, 2109–2115, https://doi.org/10.1002/qj.171.

——, and G. Magnusdottir, 2008: Tropospheric Rossby wave breaking and the NAO/NAM. *J. Atmos. Sci.*, **65**, 2861–2876, https://doi.org/10.1175/2008JAS2632.1.

Tamarin-Brodsky, T., and N. Harnik, 2023: The intrinsic relationship between cyclones, anticyclones, and Rossby wave breakings in the North-Atlantic. *EGUsphere*, https://doi.org/10.5194/egusphere-2023-534, in press.

Thorncroft, C. D., B. J. Hoskins, and M. E. McIntyre, 1993: Two paradigms of baroclinic-wave life-cycle behaviour. *Quart. J. Roy. Meteor. Soc.*, **119**, 17–55, https://doi.org/10.1002/qj.49711950903.

Tyrlis, E., and B. J. Hoskins, 2008: The morphology of Northern Hemisphere blocking. *J. Atmos. Sci.*, **65**, 1653–1665, https://doi.org/10.1175/2007JAS2338.1.

Waugh, D. W., and L. M. Polvani, 2000: Climatology of intrusions into the tropical upper troposphere. *Geophys. Res. Lett.*, **27**, 3857–3860, https://doi.org/10.1029/2000GL012250.

Wernli, H., and M. Sprenger, 2007: Identification and ERA-15 climatology of potential vorticity streamers and cutoffs near the extratropical tropopause. *J. Atmos. Sci.*, **64**, 1569–1586, https://doi.org/10.1175/JAS3912.1.

Woods, C., R. Caballero, and G. Svensson, 2013: Large-scale circulation associated with moisture intrusions into the Arctic during winter. *Geophys. Res. Lett.*, **40**, 4717–4721, https://doi.org/10.1002/grl.50912.

Woollings, T., and M. Blackburn, 2012: The North Atlantic jet stream under climate change and its relation to the NAO and EA patterns. *J. Climate*, **25**, 886–902, https://doi.org/10.1175/JCLI-D-11-00087.1.